

Weak Antilocalization in $\text{Bi}_2(\text{Se}_x\text{Te}_{1-x})_3$ Nanoribbons and Nanoplates

Judy J. Cha,[†] Desheng Kong,[†] Seung-Sae Hong,[‡] James G. Analytis,^{‡,§} Keji Lai,^{‡,||} and Yi Cui^{*,†,§}

[†]Department of Materials Science and Engineering and [‡]Department of Applied Physics, Stanford University, Stanford, California 94305, United States

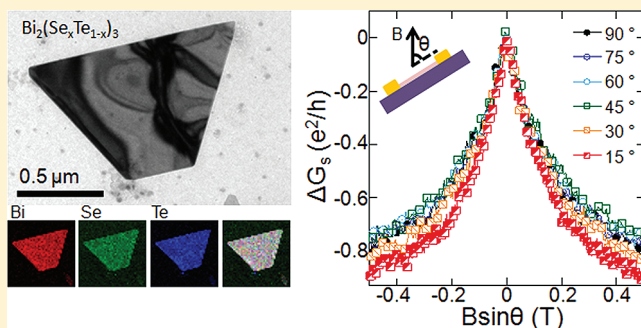
[§]Stanford Institute for Materials and Energy Sciences, SLAC National Accelerator Laboratory, 2575 Sand Hill Road, Menlo Park, California 94025, United States

^{||}Department of Physics, Stanford University, Stanford, California 94305, United States

Supporting Information

ABSTRACT: Studying the surface states of Bi_2Se_3 and Bi_2Te_3 topological insulators has proven challenging due to the high bulk carrier density that masks the surface states. Ternary compound $\text{Bi}_2(\text{Se}_x\text{Te}_{1-x})_3$ may present a solution to the current materials challenge by lowering the bulk carrier mobility significantly. Here, we synthesized $\text{Bi}_2(\text{Se}_x\text{Te}_{1-x})_3$ nanoribbons and nanoplates via vapor–liquid–solid and vapor–solid growth methods where the atomic ratio x was controlled by the molecular ratio of Bi_2Se_3 to Bi_2Te_3 in the source mixture and ranged between 0 and 1. For the whole range of x , the ternary nanostructures are single crystalline without phase segregation, and their carrier densities decrease with x . However, the lowest electron density is still high ($\sim 10^{19} \text{ cm}^{-3}$) and the mobility low, suggesting that the majority of these carriers may come from impurity states. Despite the high carrier density, weak antilocalization (WAL) is clearly observed. Angle-dependent magnetoconductance study shows that an appropriate magnetic field range is critical to capture a true, two-dimensional (2D) WAL effect, and a fit to the 2D localization theory gives α of -0.97 , suggesting its origin may be the topological surface states. The power law dependence of the dephasing length on temperature is $\sim T^{-0.49}$ within the appropriate field range ($\sim 0.3 \text{ T}$), again reflecting the 2D nature of the WAL. Careful analysis on WAL shows how the surface states and the bulk/impurity states may interact with each other.

KEYWORDS: Topological insulator, nanoribbon, bismuth selenide, bismuth telluride



The unique properties of the topological surface state such as the Dirac band dispersion and helicity^{1–3} can open many exciting opportunities for fundamental physics studies that include majorana fermions,⁴ magnetic monopole signatures,⁵ and axions⁶ as well as opportunities for applications in spintronics and quantum computing. However, there remains a significant challenge in studying and accessing the surface state of the three-dimensional (3D) topological insulators of Bi-based binary chalcogenides via transport: the residual bulk carriers that dominate the transport signal. Substitutional doping using various compensation dopants like Sn, Sb, and Ca has shown promise in reducing the bulk carrier density in Bi_2Se_3 and Bi_2Te_3 bulk crystals.^{7,8} However, to “see” the topological surface state more clearly, the bulk carrier density needs to be further reduced and currently, electrostatic gating in Bi_2Se_3 and Bi_2Te_3 thin flakes^{9,10} and $(\text{Bi}_x\text{Sb}_{1-x})_2\text{Te}_3$ nanoplates¹¹ has been tried to deplete the remaining bulk carriers and has demonstrated ambipolar field effect.

Besides lowering the bulk carrier density by substitutional doping or electrostatic gating, another way to enhance the surface state signal is if the mobility of the bulk carriers is low so that they do not interfere with quantum oscillations that

surface states may possess. Recently, $\text{Bi}_2\text{Te}_2\text{Se}_1$ and $\text{Bi}_2\text{Se}_2\text{Te}_1$ were predicted to be topological insulators,¹² and the band structure of $\text{Bi}_2\text{Te}_2\text{Se}_1$ has been measured to confirm the prediction.¹³ Furthermore, magnetotransport studies on bulk $\text{Bi}_2\text{Te}_2\text{Se}_1$ show quantum oscillations of the surface state because of the reduced contribution of bulk/impurity carriers due to the low mobility.^{14,15} For nonstoichiometric alloy $\text{Bi}_2(\text{Se}_x\text{Te}_{1-x})_3$, key factors that determine the nontrivial, topological insulator phase such as the crystal structure, spin orbit coupling strength and bulk band gap are close to those of the experimentally verified topological insulators Bi_2Se_3 and Bi_2Te_3 , thus $\text{Bi}_2(\text{Se}_x\text{Te}_{1-x})_3$ is expected to be a topological insulator for all atomic ratio x in much the same way that $(\text{Bi}_x\text{Sb}_{1-x})_2\text{Te}_3$ is a topological insulator for all x ranging between 0 and 1.^{11,16} Here, we report the synthesis of $\text{Bi}_2(\text{Se}_x\text{Te}_{1-x})_3$ nanoribbons and nanoplates and their magnetotransport properties. Because of the high surface-to-volume ratio, surface state contribution to transport may be enhanced in these nanostructures.^{17–19} We show that the atomic ratio of

Received: January 2, 2012

Se/Te in these single-crystalline nanostructures can be controlled by the molecular ratio of Bi_2Se_3 to Bi_2Te_3 in the source powder mixture and the average carrier density scales with the atomic ratio of Se/Te. Magnetotransport measurements on $\text{Bi}_2(\text{Se}_x\text{Te}_{1-x})_3$ nanoribbons show two-dimensional (2D) weak antilocalization (WAL), based on angle-dependent studies. An upper limit is set for the range of the magnetic fields appropriate for fitting the observed WAL to the 2D localization theory. Lastly, WAL was measured at different temperatures to show that the power law dependence of the dephasing length on temperature follows that of the 2D localization if the fitting range is limited to small magnetic fields up to 0.3 T.

Vapor–liquid–solid (VLS) and vapor–solid (VS) growth methods were used to synthesize $\text{Bi}_2(\text{Se}_x\text{Te}_{1-x})_3$ nanoribbons and nanoplates where a mixture of Bi_2Se_3 and Bi_2Te_3 powders was used as the precursor and their molecular ratio was varied systematically to control the composition ratio of Se/Te in the final nanostructures. Nanoribbons were grown using a 10 nm thick gold film as a metal catalyst, whereas nanoplates were grown directly on SiO_x substrates. The growth conditions for $\text{Bi}_2(\text{Se}_x\text{Te}_{1-x})_3$ nanoribbons and nanoplates are similar to the conditions for Bi_2Se_3 nanoribbons and nanoplates (also listed in Supporting Information).^{20,21} Figures 1 and 2 show the synthesized ribbons and plates respectively. The morphologies of the $\text{Bi}_2(\text{Se}_x\text{Te}_{1-x})_3$ nanoribbons (Figure 1a) and nanoplates (Figure 2a) are similar to those of Bi_2Se_3 nanoribbons and Bi_2Se_3 and Bi_2Te_3 nanoplates, displaying 60 and 120° facet angles reflective of their crystal structure. The 2D elemental maps (Figures 1b and 2b) acquired by scanning energy-dispersive X-ray spectroscopy (EDX) show that both Se and Te are evenly distributed in the nanostructures with no obvious segregations of either pure Bi_2Se_3 or Bi_2Te_3 . The composite RGB maps where Bi, Se, and Te are represented as red, green and blue, respectively, show pinkish white, corresponding to a fully mixed $\text{Bi}_2(\text{Se}_{0.43}\text{Te}_{0.57})_3$ alloy nanoribbon (Figure 1b) and $\text{Bi}_2(\text{Se}_{0.32}\text{Te}_{0.68})_3$ nanoplate (Figure 2b). The crystal structure of these nanostructures is the same as Bi_2Se_3 and Bi_2Te_3 as shown by the high-resolution TEM images and the selected-area electron diffraction patterns (Figures 1c and 2c). For the whole range of x , the ribbons and plates are found single-crystalline. The ratio x of the synthesized nanostructures scales monotonically with the molecular ratio of Bi_2Se_3 to Bi_2Te_3 in the source powder, as shown by Figures 1d and 2d (see Supporting Information Figure S1 for EDX spectra). Interestingly, the ratio x varies smoothly between 0 and 1 rather than being 1/3 or 2/3, indicating that Se and Te are randomly distributed in their sublattice sites instead of being separated into different atomic planes. The average carrier density, n_{3D} , of the $\text{Bi}_2(\text{Se}_x\text{Te}_{1-x})_3$ nanoribbons appears to decrease with x (Figure 1e). The average carrier density, n_{3D} , of the nanoplates is much higher than that of the ribbons for the same x , hence we focus our attention on the transport properties of the ribbons.

The carrier density, n_{3D} , of the $\text{Bi}_2(\text{Se}_x\text{Te}_{1-x})_3$ nanoribbons is in the range of 10^{19} cm^{-3} , much higher than doped Bi_2Se_3 bulk crystals and nanoribbons.^{8,17} Figure 3 shows magnetotransport of a typical nanoribbon device where the average x in this growth batch was 0.34 ± 0.02 , i.e. $\text{Bi}_2(\text{Se}_{0.34}\text{Te}_{0.66})_3$. Figure 3a shows the optical image of the corresponding device where six-terminal Hall bar electrodes were patterned using standard e-beam lithography, followed by thermal evaporation of Cr/Au for metal contacts. From Hall resistance at 2 K (Figure 3c), n_{2D} is $1.69 \times 10^{14} \text{ cm}^{-2}$ (corresponding n_{3D} is $1.85 \times 10^{19} \text{ cm}^{-3}$ for

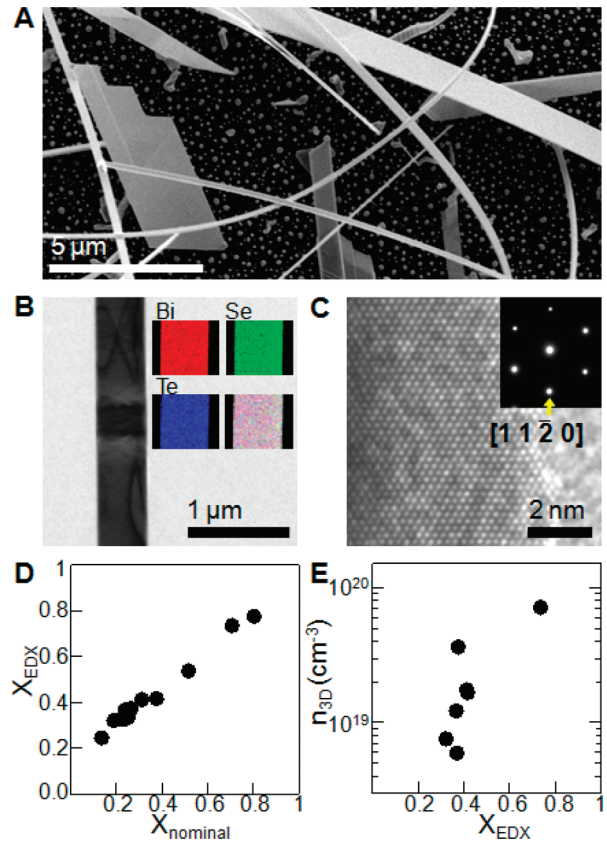


Figure 1. Synthesis of $\text{Bi}_2(\text{Se}_x\text{Te}_{1-x})_3$ nanoribbons with varying x . (A) SEM image of $\text{Bi}_2(\text{Se}_x\text{Te}_{1-x})_3$ nanoribbons where the molecular ratio $\text{Bi}_2\text{Se}_3/\text{Bi}_2\text{Te}_3$ in the source mixture was 0.6 ($x_{\text{nominal}} = 0.375$). (B) TEM image of a $\text{Bi}_2(\text{Se}_x\text{Te}_{1-x})_3$ nanoribbon. For this ribbon, x is 0.43 ± 0.02 based on EDX analysis. The insets show elemental maps of Bi (red), Se (green), and Te (blue), acquired by scanning EDX. The RGB composite image shows uniform pinkish white throughout the ribbon, indicating that Se and Te are distributed evenly in the ribbon. (C) High-resolution TEM image and selected-area diffraction pattern of the ribbon shown in B. The crystal structure of $\text{Bi}_2(\text{Se}_x\text{Te}_{1-x})_3$ nanoribbons is the same as Bi_2Se_3 and Bi_2Te_3 throughout the varying range of x . (D) Composition of x in $\text{Bi}_2(\text{Se}_x\text{Te}_{1-x})_3$ nanoribbons versus the nominal value, x_{nominal} , in the source powder mixture. Each data point is the average of tens of nanoribbons analyzed with TEM–EDX. (E) Carrier density, n_{3D} , of $\text{Bi}_2(\text{Se}_x\text{Te}_{1-x})_3$ nanoribbons as a function of x . n_{3D} is obtained by averaging the carrier densities of several devices per x .

this ~ 92 nm thick ribbon) and the Hall mobility is $28 \text{ cm}^2/(\text{Vs})$, much lower than the reported mobility of Bi_2Se_3 crystals and nanoribbons.^{22,23} Despite the high carrier density, a pronounced dip in the longitudinal resistance R near zero magnetic field, a signature of WAL, is observed (Figure 3d). Furthermore, R increases by lowering the temperature, a nonmetallic temperature behavior usually unexpected for this high carrier density (Figure 3b). The nonmetallic R versus T trace and the low Hall mobility observed in the ribbons are consistent with those reported in the bulk crystals of $\text{Bi}_2\text{Te}_2\text{Se}_1$,^{14,15} where the large number of carriers with low mobility is attributed to an impurity band that forms inside the bulk band gap.¹⁴ In the bulk crystals, Shubnikov–de Hass (SdH) oscillations of 2D nature were observed, indicating the presence of the surface state.^{14,15} In the case of the nanoribbons however, no clear SdH oscillations were observed up to 8 T magnetic fields at 2 K. We note that the electrical properties of

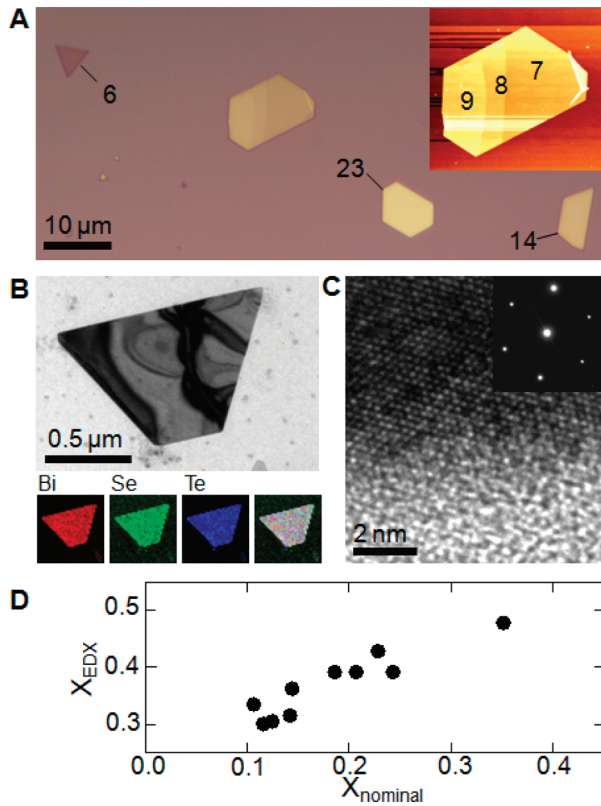


Figure 2. Synthesis of $\text{Bi}_2(\text{Se}_x\text{Te}_{1-x})_3$ nanoplates with varying x . (A) Optical image of $\text{Bi}_2(\text{Se}_x\text{Te}_{1-x})_3$ nanoplates grown on a 300 nm SiO_x substrate. These nanoplates are thin and semitransparent with distinct colors for varying thicknesses; from thin to thick plates, the color turns from purple to shiny yellow. The inset shows an atomic force microscopy image (AFM) of the plate in the center. Numbers indicate the thicknesses of the plates in nanometer, measured by AFM. (B) TEM image of a $\text{Bi}_2(\text{Se}_x\text{Te}_{1-x})_3$ nanoplate with $x = 0.32 \pm 0.02$. For TEM characterization, the plates were grown on SiN_x membrane TEM grids. The color maps are elemental distributions of Bi (red), Se (green), and Te (blue), acquired by scanning EDX. The RGB composite image shows uniform white color, indicating even distribution of Bi, Se, and Te. (C) High-resolution TEM image and selected-area diffraction pattern of the same plate. (D) Composition of x in $\text{Bi}_2(\text{Se}_x\text{Te}_{1-x})_3$ nanoplates versus the nominal value, x_{nominal} , in the source powder mixture. Each data point is the average of multiple nanoplates.

$\text{Bi}_2(\text{Se}_x\text{Te}_{1-x})_3$ nanoplates are similar to the ribbons but with much higher carrier densities.

WAL is a negative quantum correction to classical magneto-resistivity due to the wave nature of the electrons. In topological insulators, both the spin orbit coupling and the helicity of the surface state can induce WAL.^{24,25} The magnetoconductance of a wide nanoribbon was measured by tilting the ribbon at an angle, θ , with respect to the magnetic field from 0 to 90° (Figure 4a schematic). The magnetic field was perpendicular to the basal plane of the ribbon at $\theta = 90^\circ$ and in plane at $\theta = 0^\circ$. Due to the 2D nature of the surface electrons, their contribution to WAL is expected to depend only on the perpendicular component of the applied field, $B \sin(\theta)$. Because the nanoribbon is much thicker than the length scale for strong quantum confinement where the bulk states can form 2D quantum well states, bulk contributions to WAL are expected to be three-dimensional, and no weak localization is expected from bulk states.²⁶ Figure 4b shows the sheet

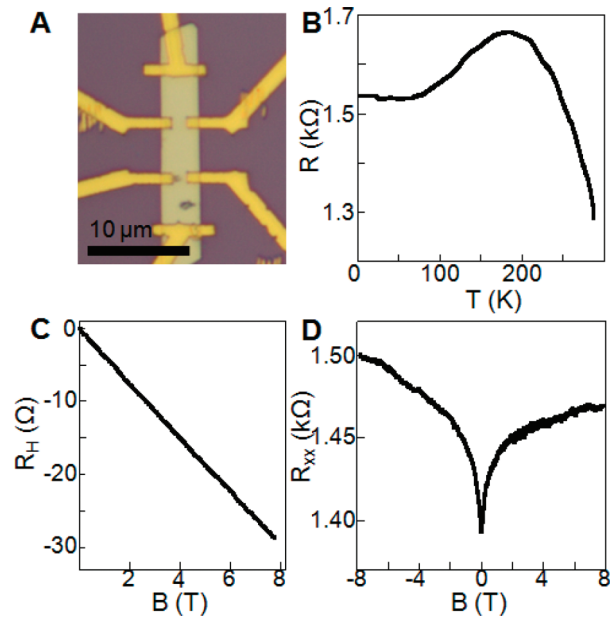


Figure 3. Magnetotransport of a $\text{Bi}_2(\text{Se}_x\text{Te}_{1-x})_3$ nanoribbon device with $x = 0.34 \pm 0.02$ at 2 K. (A) Optical image of the nanoribbon device with Hall bar electrodes. (B) Temperature dependent longitudinal resistance (R) acquired at four-point configuration, showing a nonmetallic behavior. (C) Linear Hall resistance (R_H) at 2 K. The Hall slope is $-3.69 \Omega/\text{T}$, resulting in volume carrier density of $1.85 \times 10^{19} \text{ cm}^{-3}$ for the 91.6 nm thick ribbon. (D) Longitudinal resistance (R_{xx}) in a perpendicular magnetic field. A pronounced weak antilocalization feature is observed.

magnetoconductance, G_s , of the ribbon measured at multiple θ s. WAL is observed for all angles including $\theta = 0^\circ$, indicating that both the bulk spin orbit coupling and helicity of the surface states contribute. Figure 4d shows the sheet magnetoconductance changes, $\Delta G_s = G_s - G_s(B = 0)$, plotted in $B \sin(\theta)$ (also Supporting Information Figure S2). Below 0.1 T, all traces follow a single curve, indicating WAL is essentially 2D up to 0.1 T, likely coming from the topological surface state. Figure 4c shows the trace at $\theta = 90^\circ$ with and without subtracting the trace at $\theta = 0^\circ$ that contains the bulk spin orbit coupling contribution. Up to $B = 0.1$ T, the two traces overlap, setting an upper limit for the range of the magnetic fields in which WAL is mostly 2D in nature. Our results are consistent with the previous study in Bi_2Te_3 thin films grown by molecular-beam epitaxy.²⁷

The 2D localization theory, given by $\Delta\sigma_{2D} = [-(\alpha e^2)/(2\pi^2\hbar)][\ln(B_0/B) - \psi(1/2 + (B_0/B))]$, where σ_{2D} is the 2D sheet conductance, $B_0 = \hbar/(4eL_\phi^2)$ with L_ϕ as the dephasing length, and ψ is the digamma function, describes the quantum correction to the conductivity in 2D systems.²⁴ The above equation has been used to fit experimentally observed WAL features in thin films or flakes of Bi_2Te_3 and Bi_2Se_3 and the value of α provides information about the nature of the carriers in topological insulators. A single topological surface state should give α of $-1/2$.²⁴ Experimentally, α ranges between -0.4 to -1.1 , which are attributed to a single surface state, two surface states (top and bottom surfaces), or intermixing between the bulk and surface states.^{27–31} The sheet magnetoconductance change ΔG_s (Figure 4c,d) was fitted to the above equation in the perpendicular field range up to 0.1 T where 2D WAL dominates, yielding $\alpha = -0.97$ and $L_\phi = 197$ nm. The red dotted curve in Figure 4c shows the fit. An α value of -0.97

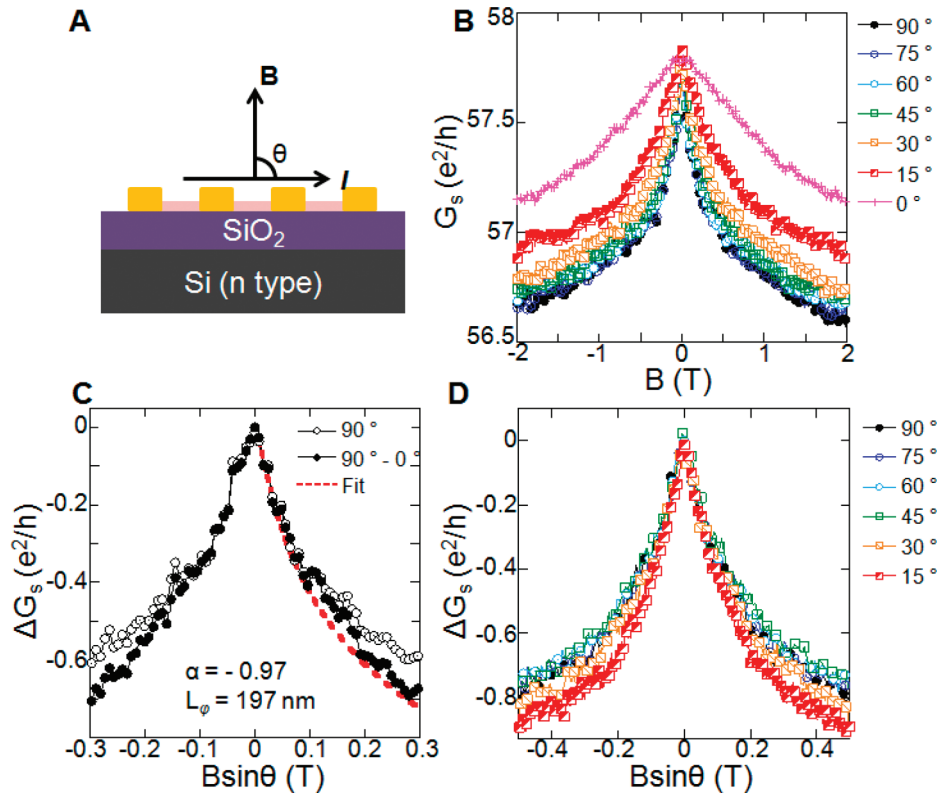


Figure 4. Angle-dependent magnetoconductance of another $\text{Bi}_2(\text{Se}_x\text{Te}_{1-x})_3$ nanoribbon device with $x = 0.34 \pm 0.02$ at 2 K. (A) Schematic of the measurement setup where θ denotes the angle between the direction of the magnetic field and the current flow in the nanoribbon. The nanoribbon device is tilted such that θ ranges between 0 and 90° . When $\theta = 90^\circ$ (0°), the magnetic field is perpendicular (parallel) to the basal planes of Bi_2Se_3 . (B) Sheet magnetoconductances at several θ s, showing the WAL feature clearly. Notice that WAL persists at $\theta = 0^\circ$, indicating that WAL is partly due to the bulk spin orbit coupling. (C) Trace at $\theta = 90^\circ$ with and without subtracting the trace at $\theta = 0^\circ$. The overlapping region between the two traces sets an upper limit for the appropriate fitting range of the magnetic field, which is (0, 0.1 T). The red dotted line is a fit to the 2D localization theory where α is -0.97 and L_φ is 197 nm. (D) Sheet magnetoconductance change plotted in the perpendicular component of the magnetic field, $B\sin\theta$. Up to 0.1 T, all the traces collapse into a single curve, indicating the 2D nature of WAL.

suggests two equivalent 2D conductive channels contributing to the observed WAL, presumably coming from the top and bottom topological surface states in this ribbon. The dephasing length, L_φ , obtained from the fit is larger than the nanoribbon thickness, thus the bulk spin orbit coupling contribution, originally expected to be 3D, is in the 2D limit (3D behavior from the bulk spin orbit coupling still exists as seen by the observed WAL at $\theta = 0^\circ$). Therefore, the pronounced WAL feature within 0.1 T is not purely due to the surface states. However, we note that the decay time associated with the spin orbit coupling (τ_{SO}) is expected to be much smaller than the decay time associated with the phase coherence (τ_φ).²⁹ When the trace at $\theta = 90^\circ$ was fitted to the equation up to 2 T, $\alpha = -0.88$ and $L_\varphi = 195$ nm, hence α deviates from -1 much more.

Magnetoconductance of the ribbon was measured at different temperatures to study the dependence of the relaxation time (or the dephasing length, $L_\varphi \propto (D\tau_\varphi)^{1/2}$ where D is a diffusion constant²⁴) on temperature. As expected, WAL disappears at higher temperatures (Figure 5a) due to the decrease of the dephasing length by increased thermal scattering. Fitting the data within the magnetic field of 0.1 T became unreliable for temperatures above 7 K, hence a larger fitting range of up to 0.3 T was used. The blue open circles in Figure 5b show the extracted values of L_φ and the blue line is the power law fit of L_φ on temperature, which gives $L_\varphi \propto T^{-0.49}$. For electron–electron scattering in 2D, the power law dependence should be $T^{-1/2}$; for scattering in 3D, it is $T^{-3/4}$.³² Hence, the temperature-

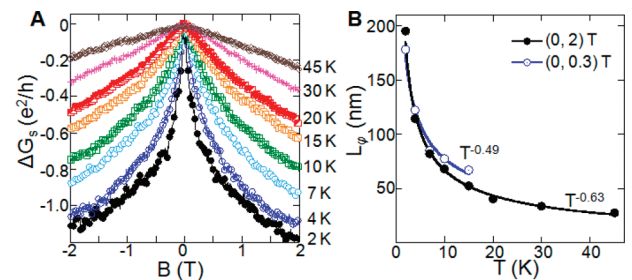


Figure 5. WAL of the nanoribbon device at higher temperatures. (A) Sheet magnetoconductances in perpendicular magnetic fields ($\theta = 90^\circ$) at temperatures ranging from 2 to 45 K. (B) L_φ as a function of temperature obtained from fitting the sheet magnetoconductance to the 2D localization theory using two different fitting ranges, (0, 0.3 T) and (0, 2 T). The solid lines show the power-law dependence on temperature. The narrower fitting range (0, 0.3 T) should capture the 2D nature of WAL while the larger fitting range (0, 2T) is expected to deviate from the 2D behavior.

dependent measurement further confirms that the WAL feature in small magnetic fields is 2D, likely due to the topological surface states. In comparison, the magnetoconductance was also fitted with the theory up to 2 T, shown as the solid black dots in Figure 5b. The magnetoconductance was found to deviate from the 2D behavior for magnetic fields larger than 0.1 T (Figure 4c,d), therefore the power law dependence of L_φ on temperature should be between that of 2D and 3D scattering

regimes. As expected, the fit (black curve in Figure 5b) gives $L_\varphi \propto T^{-0.63}$ with the exponent between $-1/2$ and $-3/4$.

In summary, we demonstrate that single-crystalline $\text{Bi}_2(\text{Se}_x\text{Te}_{1-x})_3$ nanoribbons and nanoplates can be synthesized via the VLS and VS growth methods where the range of x is tunable by the molecular ratio of Bi_2Se_3 to Bi_2Te_3 in the source powder. The carrier density scales with the ratio x , and the majority of the carriers are likely from an impurity band that has a low mobility, resulting in relative enhancement of the topological surface state despite the high carrier density, evident in the pronounced WAL feature. Angle-dependent magnetoconductance shows that WAL is 2D in nature within 0.1 T magnetic fields. Using the 2D localization theory with the fitting range limited to 0.1 T, α of -0.97 and L_φ of 197 nm are obtained. The dephasing length L_φ depends on temperature with a relation $L_\varphi \propto T^{-0.49}$ in the fitting range up to 0.3 T, confirming the 2D nature of the WAL in these $\text{Bi}_2(\text{Se}_x\text{Te}_{1-x})_3$ nanoribbons.

■ ASSOCIATED CONTENT

📄 Supporting Information

Growth conditions for $\text{Bi}_2(\text{Se}_x\text{Te}_{1-x})_3$ nanoribbons and nanoplates, EDX spectra of $\text{Bi}_2(\text{Se}_x\text{Te}_{1-x})_3$ nanoribbons with varying x , and magnetoconductance after subtracting the trace at $\theta = 0^\circ$. This material is available free of charge via the Internet at <http://pubs.acs.org>.

■ AUTHOR INFORMATION

Corresponding Author

*E-mail: yicui@stanford.edu.

■ ACKNOWLEDGMENTS

The authors thank I. Fisher for the helpful discussions. Y.C. acknowledges support from the Keck Foundation, DARPA MESO Project (No. N66001-11-1-4105), and King Abdullah University of Science and Technology (KAUST) Investigator Award (No. KUS-I1-001-12).

■ REFERENCES

- Zhang, H.; Liu, C.-X.; Qi, X.-L.; Dai, X.; Fang, Z.; Zhang, S.-C. *Nat. Phys.* **2009**, *5*, 438–442.
- Chen, Y. L.; Analytis, J. G.; Chu, J. H.; Liu, Z. K.; Mo, S. K.; Qi, X. L.; Zhang, H. J.; Lu, D. H.; Dai, X.; Fang, Z.; Zhang, S. C.; Fisher, I. R.; Hussain, Z.; Shen, Z. X. *Science* **2009**, *325*, 178–181.
- Hsieh, D.; Xia, Y.; Qian, D.; Wray, L.; Dil, J. H.; Meier, F.; Osterwalder, J.; Patthey, L.; Checkelsky, J. G.; Ong, N. P.; Fedorov, A. V.; Lin, H.; Bansil, A.; Grauer, D.; Hor, Y. S.; Cava, R. J.; Hasan, M. Z. *Nature* **2009**, *460*, 1101–1105.
- Linder, J.; Tanaka, Y.; Yokoyama, T.; Sudbø, A.; Nagaosa, N. *Phys. Rev. Lett.* **2010**, *104*, 067001.
- Qi, X.-L.; Li, R.; Zang, J.; Zhang, S.-C. *Science* **2009**, *323*, 1184–1187.
- Essin, A. M.; Moore, J. E.; Vanderbilt, D. *Phys. Rev. Lett.* **2009**, *102*, 146805.
- Hor, Y. S.; Richardella, A.; Roushan, P.; Xia, Y.; Checkelsky, J. G.; Yazdani, A.; Hasan, M. Z.; Ong, N. P.; Cava, R. J. *Phys. Rev. B* **2009**, *79*, 195208.
- Analytis, J. G.; McDonald, R. D.; Riggs, S. C.; Chu, J.-H.; Boebinger, G. S.; Fisher, I. R. *Nat. Phys.* **2010**, *6*, 960–964.
- Steinberg, H.; Gardner, D. R.; Lee, Y. S.; Jarillo-Herrero, P. *Nano Lett.* **2010**, *10*, 5032–5036.
- Yuan, H.; Liu, H.; Shimotani, H.; Guo, H.; Chen, M.; Xue, Q.; Iwasa, Y. *Nano Lett.* **2011**, *11*, 2601–2605.
- Kong, D.; Chen, Y.; Cha, J. J.; Zhang, Q.; Analytis, J. G.; Lai, K.; Liu, Z.; Hong, S. S.; Koski, K. J.; Mo, S.-K.; Hussain, Z.; Fisher, I. R.; Shen, Z.-X.; Cui, Y. *Nat. Nanotechnol.* **2011**, *6*, 705–709.
- Wang, L.-L.; Johnson, D. D. *Phys. Rev. B* **2011**, *83*, 241309.
- Xu, S.-Y.; Wray, L. A.; Xia, Y.; Shankar, R.; Petersen, A.; Fedorov, A.; Lin, H.; Bansil, A.; Hor, Y. S.; Grauer, D.; Cava, R. J.; Hasan, M. Z. arXiv:1007.5111v1, (accessed July 29, 2010).
- Ren, Z.; Taskin, A. A.; Sasaki, S.; Segawa, K.; Ando, Y. *Phys. Rev. B* **2010**, *82*, 241306.
- Xiong, J.; Petersen, A. C.; Qu, D.-X.; Cava, R. J.; Ong, N. P. arXiv:1101.1315 v1, (accessed Jan 6, 2011).
- Zhang, J.; Chang, C.-Z.; Zhang, Z.; Wen, J.; Feng, X.; Li, K.; Liu, M.; He, K.; Wang, L.; Chen, X.; Xue, Q.-K.; Ma, X.; Wang, Y. *Nat. Commun.* **2011**, *2*, 574.
- Peng, H.; Lai, K.; Kong, D.; Meister, S.; Chen, Y.; Qi, X.-L.; Zhang, S.-C.; Shen, Z.-X.; Cui, Y. *Nat. Mater.* **2010**, *9*, 225–229.
- Xiu, F.; He, L.; Wang, Y.; Cheng, L.; Chang, L.-T.; Lang, M.; Huang, G.; Kou, X.; Zhou, Y.; Jiang, X.; Chen, Z.; Zou, J.; Shailos, A.; Wang, K. L. *Nat. Nanotech.* **2011**, *6*, 216–221.
- Tang, H.; Liang, D.; Qiu, R. L. J.; Gao, X. P. *ACS Nano* **2011**, *5*, 7510–7516.
- Kong, D.; Randel, J. C.; Peng, H.; Cha, J. J.; Meister, S.; Lai, K.; Chen, Y. L.; Shen, Z. X.; Manoharan, H. C.; Cui, Y. *Nano Lett.* **2010**, *10*, 329–333.
- Kong, D.; Dang, W.; Cha, J. J.; Li, H.; Meister, S.; Peng, H.; Liu, Z.; Cui, Y. *Nano Lett.* **2010**, *10*, 2245–2250.
- Kong, D.; Cha, J. J.; Lai, K.; Peng, H.; Analytis, J. G.; Meister, S.; Chen, Y.; Zhang, H.-J.; Fisher, I. R.; Shen, Z.-X.; Cui, Y. *ACS Nano* **2011**, *5*, 4698–4703.
- Analytis, J. G.; Chu, J.-H.; Chen, Y.; Corredor, F.; McDonald, R. D.; Shen, Z. X.; Fisher, I. R. *Phys. Rev. B* **2010**, *81*, 205407.
- Hikami, S.; Larkin, A. I.; Nagaoka, Y. *Prog. Theor. Phys.* **1980**, *63*, 707–710.
- Suzuura, H.; Ando, T. *Phys. Rev. Lett.* **2002**, *89*, 266603.
- Lu, H.-Z.; Shen, S.-Q. *Phys. Rev. B* **2011**, *84*, 125138.
- He, H.-T.; Wang, G.; Zhang, T.; Sou, I.-K.; Wong, G. K. L.; Wang, J.-N.; Lu, H.-Z.; Shen, S.-Q.; Zhang, F.-C. *Phys. Rev. Lett.* **2011**, *106*, 166805.
- Chen, J.; He, X. Y.; Wu, K. H.; Ji, Z. Q.; Lu, L.; Shi, J. R.; Smet, J. H.; Li, Y. Q. *Phys. Rev. B* **2011**, *83*, 241304.
- Steinberg, H.; Laloe, J. B.; Fatemi, V.; Moodera, J. S.; Jarillo-Herrero, P. *Phys. Rev. B* **2011**, *84*, 233101.
- Zhang, G.; Qin, H.; Chen, J.; He, X.; Lu, L.; Li, Y.; Wu, K. *Adv. Func. Mater.* **2011**, *21*, 2351–2355.
- Checkelsky, J. G.; Hor, Y. S.; Cava, R. J.; Ong, N. P. *Phys. Rev. Lett.* **2011**, *106*, 196801.
- Altshuler, B. L.; Aronov, A. G. *Electron-electron interaction in disordered systems*; Elsevier Science Publishing Company: New York, 1985.